Journal of Materials Chemistry A

Accepted Manuscript

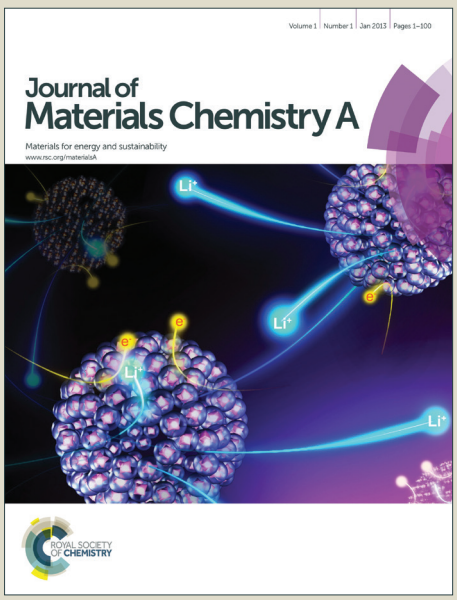

ROYAL SOCIETY OF CHEMISTRY

www.rsc.org/materialsA

Table of Contents Entry:

Internal electrical fields created in Co-doped Ta_3N_5 photoanodes facilitate hole injection into the solution phase for O_2 evolution.

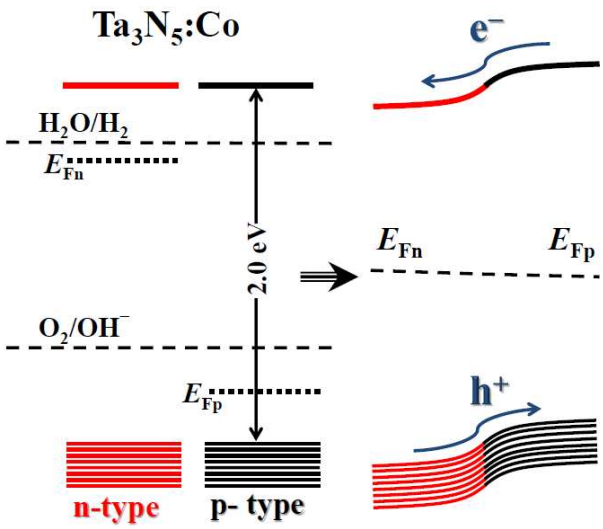

Formation of Internal P–N Junctions in Ta_3N_5 Photoanodes for Water Splitting

Yi-Chieh Wang,[1] Chih-Yung Chang,[1] Te-Fu Yeh,[1] Yuh-Lang Lee,[1] and Hsisheng Teng[1,2,*]

[1]Department of Chemical Engineering and Research Center for Energy Technology and Strategy, National Cheng Kung University, Tainan 70101, Taiwan

[2]Center for Micro/Nano Science and Technology, National Cheng Kung University, Tainan 70101, Taiwan

*To whom correspondence should be addressed. (E-mail): hteng@mail.ncku.edu.tw

(Fax): 886-6-2344496

Abstract

Tantalum nitride photoanodes for water splitting are fabricated by anodizing tantalum foils, with subsequent nitridation of the foils in NH_3. The as-synthesized Ta_3N_5 film has n-type conductivity. Loading Co ions during and after the anodization process forms a Ta_3N_5:Co film consisting of p- and n-type Ta_3N_5 domains. Both the Ta_3N_5 and Ta_3N_5:Co electrodes have a band gap of 2.0 eV. The p–n junctions in the Ta_3N_5:Co electrode create internal electrical field favorable for hole transfer from the n-type domains to the p-type. When the photoanodes are immersed in a 0.5-M KOH aqueous solution for water splitting with one-sun illumination, the Ta_3N_5:Co photoanode exhibits photocurrents an order of magnitude higher than those of the bare Ta_3N_5 photoanode. AC impedance spectroscopy analysis reveals that the p–n junctions formed by Co-doping reduce the interfacial charge transfer resistance by an order of magnitude. The diffuse reflectance spectra of the electrodes indicate that Co incorporation minimizes the defect states in the bulk Ta_3N_5. Intensity-modulated photocurrent spectroscopy analysis reveals that the high electron transit rate of the Ta_3N_5:Co electrode can be attributed to its fewer defect states. A photoelectrochemical reaction using the Ta_3N_5:Co photoanode produces H_2 and O_2 at a ratio close to 2:1, and N_2 evolution from the reaction is negligible. The present study demonstrates the establishment of a p–n junction configuration that considerably enhances the performance of nitride anodes in photocatalyzed water splitting.

Keywords: Tantalum nitride; Photoelectrode; Water splitting; Hydrogen generation; Nitride compound.

Introduction

Inducing the cleavage of water into hydrogen and oxygen gases using photoelectrochemical (PEC) and photocatalytic techniques is a promising, environmentally friendly solar fuel production method.[1–13] Several n-type metal-oxide semiconductors (e.g., WO_3,[14,15] Fe_2O_3,[16] and $BiVO_4$[17]) have been used as photoanodes for water oxidation, but further improvement in their overall water-splitting operation in visible light is necessary. Transitional metal (oxy)nitrides have attracted considerable attention as potential visible-light-driven photocatalysts;[18–21] tantalum nitride (Ta_3N_5) is a prospective candidate for this, with a band gap of approximately 2 eV, and conduction band minimum (CBM) and valence band maximum (VBM) levels appropriate for photocatalytic water splitting to produce both H_2 and O_2.[22,23] However, most nitrides undergo self-oxidative decomposition through the oxidation of nitrogen anions by photogenerated holes to N_2 (that is, $2\ N^{3-} + 6\ h^+ \rightarrow N_2$).[24–26] To improve the PEC performance of Ta_3N_5, a strategy must be designed for effectively transporting photogenerated holes for oxygen evolution.[27–32]

N-type semiconductors, such as Ta_3N_5, create depleted space-charge regions when brought into contact with water. Because of the strong electrical field in the space-charge region, photogenerated holes migrate toward the interface while electrons migrate toward the interior. Applying anodic bias on the photoanode augments the electrical field in the space-charge region, thereby enhancing charge separation to give high photocurrents. However, applying an external bias causes a tradeoff between the power output required for water splitting and the external power supplied in converting light energy.[5,33,34] Constructing a built-in electrical field on the surface of the semiconductor electrode may alleviate the external bias required in

water splitting. Previous studies have shown that surface modification of a Ta_3N_5 photoelectrode with Co-based materials or IrO_2 effectively promotes hole injection into the liquid phase, thereby stabilizing the Ta_3N_5 electrode.[31,32,35,36] Because a Co atom has fewer valence electrons (2 or 3) than Ta, doping Co may introduce p-type conductivity to a Ta_3N_5 electrode, which is intrinsically n-type, and construct p–n junctions in the Ta_3N_5 electrode to facilitate hole transfer for O_2 evolution.

In this study, we synthesized an n-type Ta_3N_5 thin-film photoanode by anodizing a Ta foil to form Ta_2O_5 with subsequent annealing of the foil in ammonia. By loading Co ions on Ta_2O_5 in situ during Ta-foil anodization with subsequent soaking of the foil in $Co(NO_3)_2$, we produced p-type domains embedded in Ta_3N_5 by annealing the Co-loaded Ta_2O_5 film in ammonia. We proposed that homojunctions were formed between the p-type and n-type domains on the Co-loaded Ta_3N_5 (i.e., Ta_3N_5:Co) electrode, and discovered that implanting p-type domains onto the n-type Ta_3N_5 electrode enormously enhanced its water splitting performance under illumination. The internal electric field created in the p–n junction facilitated the separation of photogenerated electron–hole pairs and external cobalt-oxide species (CoO_x) facilitated hole transfer for O_2 evolution. A detailed characterization regarding the p–n junction of this nitride photoelectrode and a discussion of the charge transfer mechanism are presented in this paper.

Experimental Section

The Ta_3N_5 films were prepared by electrochemically anodizing a 1-cm^2 Ta foil (Sigma Aldrich, 99.9% purity) followed by annealing in anhydrous ammonia gas.

Prior to anodization, the Ta foil was cleaned sonicating it in acetone (J.T. Baker, 99.9% purity), methanol (Fisher Scientific, 99.9% purity), and isopropanol (J.T. Baker, 99.9% purity), and then dried in air. The electrolyte solution for anodization consisted of 1 wt% NH_4F (Alfa Aesar, 96% purity) and 1 vol% H_3PO_4 (Hokwang, 85% purity) dissolved in ethylene glycol (J.T. Baker, 99.9% purity).[37,38] The cleaned Ta foil was anodized at 30 V for 5 min at 20 °C to form a Ta_2O_5 film, which was then annealed in a tube furnace at 950 °C under an anhydrous-ammonia flow of 100 mL min^{-1} for 2 h to create a Ta_3N_5 film. To synthesize a Ta_3N_5:Co film, we anodized a Ta foil in the electrolyte solution, adding 0.083 wt% $Co(NO_3)_2$ (Alfa Aesar, 98% purity) to load Co ions in situ, and then soaked the resulting Ta_2O_5 film in a 0.5 M-$Co(NO_3)_2$ methanol solution for 5 min. The air-dried Co-loaded Ta_2O_5 film was annealed at 950 °C in anhydrous ammonia for 2 h to obtain a Ta_3N_5:Co film.

The crystal structure of the nitride films was characterized by performing X-ray diffraction (XRD) using a diffractometer (Rigaku Ultima IV) with Cu Kα radiation, excited at 40 kV and 40 mA. The XRD patterns were collected at 2θ angles of 20°–70° and the scan rate was 4° min^{-1}. The morphology of the samples was characterized using high-resolution transmission electron microscopy (HR-TEM; Jeol JEM-2100F), which was equipped with an auxiliary for energy dispersive X-ray spectroscopy (EDS) analysis on the chemical composition. X-ray photoelectron spectroscopy (XPS; Kratos AXIS Ultra DLD) with Al K_α radiation was used to quantitatively analyze the chemical composition of the nitride films. The diffuse reflection spectra for the specimens were measured using an ultraviolet-visible-near-infrared (UV-Vis-NIR) spectrometer (Hitachi U-4100) equipped with an integration sphere, and the spectra were converted from reflection to absorbance spectra by using the Kubelka-Munk method.[39,40]

The conductivity-type and Fermi level potential of the electrodes were analyzed by performing electrochemical impedance spectroscopy (EIS) using an impedance spectrum analyzer (Zahner IM6e) equipped with Thales software. The measurement process involved applying a sinusoidal potential perturbation with a small amplitude (10 mV) at each potential to obtain the capacitance of the space-charge region in a 0.5 M-KOH (Merk, > 84% purity) solution, using a platinum sheet as the counter electrode. We used a linear potential scan, 10 mV s^{-1}, in the same electrochemical system to determine the VBM of the Ta_3N_5 electrode.

The PEC water-splitting reactions were executed in a two-armed cell equipped with a quartz window, using an Ag/AgCl reference electrode and a platinum sheet as the counter electrode. The electrolyte was a 0.5-M KOH aqueous solution, with a pH value of approximately 13.6. The photoelectrodes were illuminated with chopped AM 1.5G simulated sunlight at 100 mW cm^{-2}. Photocurrent-voltage characteristics were recorded by using an electrochemical analyzer (CH Instruments 614B), applying a linear scan from –0.4 to 0.6 V (vs. Ag/AgCl) at 10 mV s^{-1}. The bias potentials between the working and counter electrodes were measured for calculating the photon-to-current conversion efficiency.[41] The charge transfer resistance for water splitting on the electrode surface was measured using EIS at 0.5 V (vs. Ag/AgCl) in an AC frequency range of 0.1–10^5 Hz. We analyzed the electron transport dynamics by using intensity-modulated photocurrent spectroscopy (IMPS) with a frequency response analyzer (Zahner XPOT), which also drove a blue light-emitting diode (λ = 455 nm) at a DC light intensity of 15 mW cm^{-2}. The light intensities were modulated (5%) by adjusting the voltage applied to the diode with sinusoidal waves in a frequency range of 0.1–10^5 Hz. The hydrogen and oxygen evolved by the PEC water splitting was measured by performing gas chromatography (Hewlett-Packard 7890;

molecular sieve 5A column, thermal conductivity detector, argon carrier gas).

Results and Discussion

Fig. 1 shows the XRD patterns of the Ta_3N_5 and Ta_3N_5:Co films obtained from nitridation in NH_3 at 950 °C for 2 h. The main phase of the Ta_3N_5 film was characterized by an orthorhombic structure (JCPDS 79-1533, the standard pattern depicted at the bottom of Fig. 1). The main phase of the Ta_3N_5:Co film was also characterized by the orthorhombic structure of Ta_3N_5, but showed additional peaks at 2θ values of 44° and 51° that correspond to the diffraction of the cubic $Co_{5.47}N$ crystal (JCPDS 41-0943, the standard pattern depicted in the upper part of Fig. 1). However, the diffraction peaks of the $Co_{5.47}N$ contained in the Ta_3N_5:Co film were dull. Fig. 2 shows a high-resolution TEM image of a Ta_3N_5:Co particulate specimen scraped from the as-synthesized Ta_3N_5:Co film. The particulate specimen consisted of a small particle that was approximately 5 nm, in intimate contact with a large particle that was 20–30 nm. The small particle exhibited a lattice spacing distance of 0.207 nm that was identical to that of the $Co_{5.47}N$ (111) plane, and the large particle exhibited spacing distances of 0.280 and 0.228 nm that were identical to those of the Ta_3N_5 (023) and (024) planes, respectively. The TEM image reveals that the Ta_3N_5:Co film consisted of small $Co_{5.47}N$ nanoparticles decorating the external surface of the bulk Ta_3N_5.

The EDS analysis on the Ta_3N_5:Co sample revealed a Co/Ta atomic ratio of approximately 0.1. The $Co_{5.47}N$ nanocrystals present on the external surface of the Ta_3N_5:Co particles could not account for this Co content because their corresponding

peaks were dull in the XRD pattern of the Ta_3N_5:Co sample. The results of the EDS and XRD analyses indicate that the majority of Co ions were distributed in the bulk Ta_3N_5 instead of crystallized to $Co_{5,47}N$. In the synthesis of the Ta_3N_5:Co photoanode, soaking the Ta_2O_5 film in the $Co(NO_3)_2$ solution might result in the forming the crystalline $Co_{5,47}N$ on the sphere surface, whereas Co ions introduced in situ during anodization might have been dissolved into the Ta_3N_5 lattice.

Fig. 3 shows the optical absorbance of nitride films converted from the diffuse reflectance spectra. Both the Ta_3N_5 and Ta_3N_5:Co specimens had absorption edges at approximately 620 nm, corresponding to a band-gap value of 2.0 eV. The steep onset of light absorption by both specimens can be attributed to electron transitions from the N 2p orbitals to the empty Ta 5d orbitals,[42] whereas absorption by Ta_3N_5:Co at longer wavelengths ($\lambda > 650$ nm) indicates the presence of surface defects that created localized states within the Ta_3N_5 band gap. The external Co deposition should be responsible for this defect-state absorption. However, the absorption resulting from electron transitions across the band gap ($\lambda < 600$ nm) was also stronger for Ta_3N_5:Co relative to that of bare Ta_3N_5. This strong gap-transition absorption by Ta_3N_5:Co indicates a low defect-state density in the material bulk. Because Co ions were incorporated into the Ta_3N_5 lattice in Ta_3N_5:Co, the lower valence of Co ions relative to that of Ta ions might have resulted in eliminating Ta^{4+}-related defect states caused by the intrinsic nitrogen vacancy in the Ta_3N_5 bulk. Eliminating defect states located in the electrode bulk is beneficial to photogenerated electron transport, which involves diffusion in the conduction band and trapping-detrapping by defect states.[43]

The band gap energy of Ta_3N_5 was sufficiently high to overcome the theoretical endothermic 1.23 eV requirement for the water-splitting reaction. The CBM and VBM levels of Ta_3N_5 relative to those for water reduction and oxidation, respectively,

influence the effective generation of H_2 and O_2 in water splitting. We conducted EIS analysis on the synthesized Ta_3N_5 and Ta_3N_5:Co film electrodes to identify the electronic characteristics based on the Mott-Schottky equation:[44–46]

$$\frac{1}{C^2} = \frac{2}{e\varepsilon\varepsilon_0 N_A}(E - E_F - \frac{kT}{e})$$

where C represents the capacitance of the space-charge region, ε_0 is the vacuum permittivity, ε is the dielectric constant of the catalyst, e is the electron charge, E is the applied potential, E_F is the Fermi level, k is the Boltzmann constant, T is the absolute temperature, and N_A is the acceptor density (or donor density). The temperature term is generally small and can be neglected. Fig. 4 shows the capacitance values of the space-charge region obtained at various applied potentials. According to the Mott-Schottky equation, $1/C^2$ vs. E exhibits a linear relationship. The positive slope observed in Fig. 4a conclusively determined the n-type conductivity of the Ta_3N_5 film. In the plot for the Ta_3N_5:Co film (Fig. 4b), the linear lines with negative and positive slopes located in different potential regimes indicate the coexistence of both p- and n-type conductivities. The results indicated that doping the lower-valence Co element into the nitride framework of the higher-valance Ta (i.e., Ta_3N_5) resulted in p-doping and formation of p-type domains over the outer part of the n-type Ta_3N_5, but the p-domains did not entirely cover the n-type Ta_3N_5 surface. Both the n- and p-domains were in contact with the electrolyte solution. The capacitance values of the space-charge regions in the n- and p-domains were equal at the crossing point of positive and negative slope in the Mott-Schottky plot of Fig. 4b. The crossing point represents the potential for the changeover of the dominant conductivity-type of the electrode.

Auxiliary experiments showed that both the Co-loading steps, during and after

the anodization process, must be applied to obtain films containing both p- and n-type conductivity. Loading Co ions either during or after anodization obtained only n-type films. Therefore, soaking the Ta_2O_5 film in the $Co(NO_3)_2$ solution with subsequent nitridation might cause Co-ion diffusion into the Ta_3N_5 lattice and create p-type domains in the outer part of the Ta_3N_5 sphere. The concentration of the $Co(NO_3)_2$ soaking solution governed the Co-doping degree (i.e., the acceptor content) and, therefore, influenced the PEC performance of the resulting films (Fig. S1 of the ESI†). The present work used the optimized $Co(NO_3)_2$-solution concentration. Since the Ta_3N_5:Co film was constituted by a homogeneous Ta_3N_5 framework, homojunctions, which would be less resistive for charge motion,[44,47] were created at the interface between the p- and n-type domains. The crystalline $Co_{5.47}N$ formed on the external surface of Ta_3N_5:Co particles were not involved in this conductivity conversion. The $Co_{5.47}N$ was oxidized to oxide species CoO_x under a positive potential bias in a PEC system. Fig. S2 of the ESI† shows the Co $2p_{3/2}$ XPS spectra of the Ta_3N_5:Co film. Low-valence Co ions, likely belonging to $Co_{5.47}N$, were observed for the as-received Ta_3N_5:Co film (Fig. S2a), and the Co ions were oxidized to high-valence ions, likely belonging to Co_2O_3/Co_3O_4 (i.e., CoO_x), after the PEC reaction (Fig. S2b). The CoO_x species might then serve as a cocatalyst for O_2 evolution in a PEC water-splitting reaction.[31,36,48,49]

The Fermi levels of the materials, E_{Fn} and E_{Fp} for n- and p-type conductivities, respectively, were determined based on the intercepts of the extrapolated straight lines on the abscissa. Fig. 4 shows an E_{Fn} level of –0.92 V (vs. Ag/AgCl) for the Ta_3N_5 film and a similar value for the n-type conductivity of the Ta_3N_5:Co film, which had an E_{Fp} value of 0.39 V (vs. Ag/AgCl). We used a linear potential scan to determine the VBM energy levels of the Ta_3N_5 (or Ta_3N_5:Co) film. Applying potentials below the VBM

for n-type materials to form an inversion layer can lead to the abrupt emergence of an irreversible anodic current.[50,51] Fig. 5 shows the application of an anodic scan on the n-type Ta_3N_5 film without illumination. The abrupt current increase yielded a VBM of 0.7 V (vs. Ag/AgCl) for Ta_3N_5. By summarizing the data from the optical and electrochemical measurements, we constructed energy level diagrams for the Ta_3N_5:Co film, as shown in Fig. 6a, which also depict the potentials for H_2 and O_2 evolution from water decomposition. The band gap of the Ta_3N_5:Co film encompassed the water-redox potentials, indicating the feasibility of this film to serve as media in PEC water splitting. Fig. 6a reveals the neutral situation of the p- and n-type domains. Because p–n junctions would be formed in the Ta_3N_5:Co film, Fig. 6b shows that the neutrality was disturbed and Fermi-level alignment of the p- and n-type domains occurred to create a built-in field at the interface and rectified the transport of photogenerated charges.

In an n-type photoanode (such as Ta_3N_5) in a PEC water-splitting system, photogenerated electrons must travel through the conduction band of the semiconductor film before being collected by the collector (in this case, the Ta foil); the holes transport through the valence band to the photoanode surface for water oxidation. The challenge for nitride-based photoanodes is that holes tend to oxidize the nitrides by reacting with nitrogen ions, especially when the holes cannot be effectively transferred out of the surface.[24] Introducing p-type conductivity in the exterior of the n-type photoanode may facilitate the vectorial charge displacement for water splitting. The configuration of the p–n junction shown in Fig. 6b is therefore beneficial for transferring holes generated in the n-type domain out of the photoanode through the p-type domain.

We subjected the Ta_3N_5 and Ta_3N_5:Co film electrodes to PEC analysis in a 0.5-M

KOH solution. Fig. 7 shows the photocurrent-potential responses of the electrodes with an anodic scan applied at 10 mV s^{-1} and illuminated with chopped AM1.5 simulated sunlight at 100 mW cm^{-2}. Both electrodes exhibited photocurrents that increased with the anodic bias, revealing the n-type conductivity of the electrodes. These photocurrent-potential responses remained stable when the electrodes were subjected to repeated potential scans. Introducing Co ions into the Ta_3N_5 structure markedly increased the photocurrents by one order of magnitude; for example, the photocurrent of Ta_3N_5:Co reached 2.5 mA cm^{-2} at 0.5 V (vs. Ag/AgCl), which was approximately 12 times higher than that of bare Ta_3N_5. This prominent enhancement in photocurrent can be attributed to the formation of the p–n junction between p- and n-type domains in the Ta_3N_5:Co film (see Fig. 6). The junction enabled the effective separation of photogenerated charges that are otherwise wasted in recombination. We did not ruled out the possibility that the CoO_x species formed on the external surface acted as a cocatalyst for O_2 evolution.[31,36,48,49] However, the formation of the p–n junction was essential for the prominent enhancement in photocurrent because loading CoO_x species on a Ta_3N_5 film did not substantially enhance the photocurrent. Figure 7 demonstrates that the photocurrent of a Ta_3N_5 film deposited with CoO_x (CoO_x-Ta_3N_5) was larger than that of the bare Ta_3N_5 film but was much smaller than that of Ta_3N_5:Co. In addition, Fig. S3 of the ESI† shows that the Ta_3N_5:Co electrode exhibits a much higher photocurrent in a fast polysulfide redox couple (S^{2-}/S_x^{2-}), reflecting the effect of the p-n junction independently of the electrocatalytic effect of the CoO_x.

The p-type domain in the Ta_3N_5:Co film was created in the outer part of the Ta_3N_5 framework and the inner n-type domain directly connected with the current collector, i.e. the Ta foil. Fig. 6 reveals that the p–n junction rectifies the flow of photogenerated electrons from the p-domain to n-domain, then to the Ta foil, while

directs the flow of holes from the n-domain to p-domain. This junction obstructed the flow of holes from the p-domain to n-domain and, therefore, p-type photoresponse was not observed in the current-potential curve of Fig. 7. A previous study by Wang and Osterloh also reported this situation for a photocatalyst containing a p–n junction (i.e., a Co_3O_4–$BiVO_4$ junction).[52]

The applied bias photo-to-current conversion efficiency (η) of the Ta_3N_5:Co photoanode is calculated using the following equation,[41]

$$\eta\,(\%) = [J_p \times (1.23 - |E_b|) / Int] \times 100$$

where J_p (mA cm^{-2}) is the photocurrent density, *Int* (mW cm^{-2}) is the intensity of incident light, and E_b is the applied bias (V) between the working and counter electrodes. Fig. S4 of ESI† shows the η value of the Ta_3N_5:Co photoanode, which is calculated as 1.7 % at a bias of 0.53 V vs. counter (or 0.39 V vs. Ag/AgCl) using the data of Fig. 7. We tested the stability of the Ta_3N_5:Co photoanode by conducting the photoelectrochemical reaction at the optimal bias (0.39 V vs. Ag/AgCl) for a long period of time. Fig. S5 of ESI† presents a stable photocurrent with little decay, indicating the anodic photocurrent is not due to oxidation of cobalt species at the Ta_3N_5 surface but due to the oxidation of water.

To explore the charge transport dynamics in the electrodes, we used EIS to analyze electrodes biased at 0.5 V (vs. Ag/AgCl) and illuminated under simulated sunlight at 100 mW cm^{-2}.[53,54] Fig. 8a shows the Nyquist impedance spectra of the Ta_3N_5 and Ta_3N_5:Co film electrodes analyzed in a frequency range of 0.1–10^5 Hz. The inset reveals the magnification of the zone close to the origin. The spectrum of the Ta_3N_5 electrode exhibited an arc with a much larger diameter than that of the Ta_3N_5:Co electrode; this large arc diameter indicated the large resistance of the electrodes to charge transfer. The impedance spectra were simulated and interpreted

using an equivalent circuit (Fig. 8b), in which R_s was the solution resistance and the *RC* loop, consisting of a capacitance C_{ct} and a resistance R_{ct}, characterized the charge transfer behavior across the electrode-solution interface. The fitted R_{ct} values were 18 and 0.70 kΩ for the Ta_3N_5 and Ta_3N_5:Co electrodes, respectively. The R_{ct} value of the Ta_3N_5:Co electrode was an order of magnitude smaller than that of the Ta_3N_5 electrode, confirming that the presence of the p–n junction, which facilitated charge transfer across the interface, was the major reason for the high photocurrent of the Ta_3N_5:Co electrode.

Because transport dynamics are associated with defect-state density, the effect of the introduction of Co ions on electron transport in the Ta_3N_5 film required further exploration.[15,55,56] We subjected the Ta_3N_5 and Ta_3N_5:Co films to analysis with IMPS, which measures the photocurrent response to modulation in incident light intensity.[57–59] During the IMPS measurements, the Ta_3N_5 and Ta_3N_5:Co electrodes were biased at 0.5 V (vs. Ag/AgCl) and illuminated with a blue light-emitting diode (λ_{max} = 455 nm) at 15 mW cm^{-2}. Fig. 9 shows the real and imaginary components of the photomodulated currents, Re(*J*) and Im(*J*), respectively, at a varying modulation frequency *f*. The IMPS spectra exhibited a semicircular feature in the complex plane, indicating that a uniform electron diffusion pattern characterized electron transport in the films.[60] We estimated the average transit time (τ_d) of the photogenerated electron in the electrodes according to the relation $\tau_d = (2\pi f_{min})^{-1}$, where f_{min} is the frequency at the minimum Im(*J*) observed in the IMPS plot.[59] The average transit times for the Ta_3N_5 and Ta_3N_5:Co films were 42 and 33 ms, respectively; the Ta_3N_5:Co film exhibited a higher electron transit rate than the Ta_3N_5 film did. This higher electron transport rate may result from the elimination of defect states in the Ta_3N_5 bulk with Co ion incorporation. As shown in Fig. 3, the diffuse reflectance spectra revealed that

Co introduction enhanced gap-transition absorption by Ta_3N_5 due to defect-state elimination. This IMPS analysis reflects the importance of incorporating Co ions during the anodization process. Our auxiliary experiments showed that high photocurrents could not be obtained in PEC tests without this Co ion incorporation step.

We analyzed the gases evolved from the reaction cell in a two-electrode water-splitting reaction using the Ta_3N_5:Co electrode biased at 0.8 V (vs. Pt). Fig. 10 shows the time courses of the accumulated amounts of H_2 and O_2 evolution and the half amount of electrons measured using the external circuit ($e^-/2$). The ratio of evolved H_2 and O_2 was close to 2:1. The O_2 evolution required a long induction time. The N_2 evolution diminished quickly in the early stage of the measurement and the anodic photocurrent still remained constant throughout the measurement, indicating that the anodic photocurrent was due to oxidation of water. The mole number of evolved H_2 amounted to half that of the electrons passing through the outer circuit, reflecting that the photocurrents resulted entirely from the water-splitting redox reactions and the undesirable backward reaction between H_2 and O_2 was negligible. The negligible amount of N_2 evolution revealed that the p–n junction facilitated hole injection into the aqueous solution and suppressed self-oxidation of the nitride electrode.

Conclusions

This study demonstrated that introducing Co ions to create p-type domains in an n-type Ta_3N_5 photoanode effectively enhanced the activity of the Ta_3N_5 anode in PEC

water splitting. Electronic structure analysis revealed that the band gap of the Ta_3N_5:Co film encompassed the water-redox potentials and the built-in electrical field created in the resulting p–n junction facilitated hole transport from interior n-type domains out of the photoanode through p-type domains. The Ta_3N_5:Co electrode exhibited water-splitting activity an order of magnitude higher than that of the Ta_3N_5 electrode. EIS analysis revealed that the incorporation of Co ions reduced the charge transfer resistance of the Ta_3N_5 electrode by an order of magnitude, confirming that the p–n junction facilitated injection of photogenerated holes into the solution phase. Optical absorption measurements showed that Co-ion incorporation enhanced gap-transition absorption by Ta_3N_5, indicating minimization of the Ta^{4+}-related defect states in the Ta_3N_5 bulk. IMPS analysis revealed a swift transit of electrons in the Ta_3N_5:Co electrode, confirming that the incorporation of Co ions induced the removal of defect states. The present study developed a strategy to enhance the activity of a nitride photoanode by creating p–n homojunctions in the anode. The junctions facilitated hole transfer across the electrode-solution interface and electron transport toward the current collector. The charge transfer enhancement also suppressed self-oxidation of the nitride compounds.

Acknowledgments

This research is supported by the National Science Council of Taiwan (101-2221-E-006-243-MY3, 101-2221-E-006-225-MY3, 102-3113-P-006-012, and 102-3113-E-006-002) and the “Aim for the Top-Tier University and Elite Research Center Development Plan” of National Cheng Kung University. We are thankful to

Mrs. Shih-Wen Tseng of Center for Micro/Nano Science and Technology for assisting HR-TEM analysis.

† **Electronic Supplementary Information (ESI) available**: the influence of the Co-doping degree on the photoelectrochemical performance of the Ta_3N_5-based photoanodes; the Co $2p_{3/2}$ XPS spectra of the Ta_3N_5:Co film; the photocurrents exhibited by the bare Ta and the Ta_3N_5:Co electrodes in a polysulfide redox couple (S^{2-}/S_x^{2-}) solution; calculation of solar energy conversion efficiency of the Ta_3N_5:Co photoanode; a stability test of the Ta_3N_5:Co electrode by conducting a long-time photoelectrochemical reaction. See DOI: 10.1039/b000000x/.

References

1. C. Santato, M. Ulmann and J. Augustynski, *Adv. Mater.* 2001, **13**, 511-514.
2. J. Akikusa and S. U. M. Khan, *Int. J. Hydro. Energy* 2002, **27**, 863-870.
3. J. H. Park and A. J. Bard, *Electrochem. Solid State Lett.* 2006, **9**, E5-E8.
4. Y. H. Hu, *Angew. Chem. Int. Edit*. 2012, **51**, 12410-12412.
5. M. G. Walter, E. L. Warren, J. R. McKone, S. W. Boettcher, Q. Mi, E. A. Santori and N. S. Lew, *Chem. Rev.* 2010, **110**, 6446-6473.
6. T. K. Townsend, N. D. Browning and F. E. Osterloh, *Energy Environ. Sci*. 2012, **5**, 5943-5950.
7. K. H. Chung, M. M. Rahman, H. S. Son and J. J. Lee, *Int. J. Photoenergy* 2012, **2012**, 1-6.
8. C. Santato, M. Odziemkowski, M. Ulmann and J. Augustynski, *J. Am. Chem. Soc.* 2001, **123**, 10639-10649.
9. T. L. Li and H. Teng, *J. Mater. Chem.* 2010, **20**, 3656-3664.
10. T. F. Yeh, J. M. Syu, C. Cheng, T. H. Chang and Teng, H. *Adv. Funct. Mater.* 2010, **20**, 2255-2262.
11. T. L. Li, Y. L. Lee and H. Teng, *J. Mater. Chem.* 2011, **21**, 5089-5097.
12. K. Iwashina and A. Kudo, *J. Am. Chem. Soc.* 2011, **133**, 13272-13275.
13. Q. X. Jia, K. Iwashina and A. Kudo, *Proc. Natl. Acad. Sci. U. S. A.* 2012, **109**, 11564-11569.
14. C. Santato, M. Ulmann and J. Augustynski, *J. Phys. Chem. B* 2001, **105**, 936-940.
15. P.T. Hsiao, L.C. Chen, T.L. Li and H.S. Teng, *J. Mater. Chem.* 2011, **21**, 19402-19409.
16. A. Kay, I. Cesar and M. Grätzel, *J. Am. Chem. Soc.* 2006, **128**, 15714-15721.
17. K. Sayama, A. Nomura, T. Arai, T. Sugita, R. Abe, M. Yanagida, T. Oi, Y.

Iwasaki, Y. Abe and H. Sugihara, *J. Phys. Chem. B* 2006, **110**, 11352-11360.

18. S. S. K. Ma, K. Maeda, T. Hisatomi, M. Tabata, A. Kudo and K. Domen, *Chem. Euro. J.* 2013, **23**, 7480-7486.
19. A. Kudo and Y. Miseki, *Chem. Soc. Rev.* 2009, **38**, 253-278.
20. Q. H. Zhang and L. Gao, *Langmuir* 2004, **20**, 9821-9827.
21. R. Abe, M. Higashi and K. Domen, *J. Am. Chem. Soc.* 2010, **132**, 11828-11829.
22. A. B. Murphy, P. R. F. Barnes, L. K. Randeniya, I. C. Plumb, I. E. Grey, M. D. Horne and J. Glasscock, A. *Int. J. Hydro. Energy* 2006, **31**, 1999-2017.
23. M. Yashima, Y.G. Lee and K. Domen, *Chem. Mater.* 2007, **19**, 588-593.
24. D. Yokoyama, H. Hashiguchi, K. Maeda, T. Minegishi, T. Takata, R. Abe, J. Kubota and K. Domen, *Thin Solid Films* 2011, **519**, 2087-2092.
25. M. Higashi, K. Domen and R. Abe, *Energy Environ. Sci.* 2011, **4**, 4138-4147.
26. T. Takata, G. Hitoki, J. Kondo, M. Hara, H. Kobayashi and K. Domen, *Res. Chem. Intermed.* 2007, **33**, 13-25.
27. J. Wang, D. N. Tafen, J. P. Lewis, Z. Hong, A. Manivannan, M. Zhi, M. Li and N. Q. Wu, *J. Am. Chem. Soc.* 2009, **131**, 12290-12297.
28. N. Q. Wu, J. Wang, D. Tafen, H. Wang, J. G. Zheng, J. P. Lewis, X. Liu, S. S. Leonard and A. Manivannan, *J. Am. Chem. Soc.* 2010, **132**, 6679-6685.
29. M. Liao, J. Feng, W. Luo, Z. Wang, J. Zhang, Z. Li, T. Yu and Z. Zou, *Adv. Funct. Mater.* 2012, **22**, 3066-3074.
30. A. Ishikawa, T. Takata, J. N. Kondo, M. Hara and K. Domen, *J. Phys. Chem. B* 2004, **108**, 11049-11053.
31. M. Li, W. Luo, D. Cao, X. Zhao, Z. Li, T. Yu and Z. Zou, *Angew. Chem. Int. Edit.* 2013, **52**, 11016-11020.
32. Y. Cong , H. S. Park , H. X. Dang ,F. F. Fan , A. J. Bard *, and C. B. Mullins, *Chem.*

Mater. 2012, **24**, 579-586.

33. A. Paracchino, V. Laporte, K. Sivula, M. Grätzel and E. Thimsen, *Nat. Mater.* 2011, **10**, 456-461.
34. Z.S. Li, W.J. Luo, M.L. Zhang, J.Y. Feng and Z.G. Zou, *Energy Environ. Sci*. 2013, **6**, 347-370.
35. Y. Li, T. Takata, D. Cha, K. Takanabe, T. Minegishi, J. Kubota and K. Domen, *Adv. Mater.* 2013, **25**, 125-131.
36. G.M Wang, Y.C. Ling, H.Y. Wang, X.H. Lu and Y. Li, *J. Photochem. Photobiol. C* 2014, **19**, 35-51.
37. W. Wei, J. M. Macak, N. K. Shrestha and P. Schmuki, *J. Electrochem. Soc.* 2009, **156**, K104-K109.
38. R. Liu, W. D. Yang, L. S. Qiang and J. F. Wu, *Thin Solid Films* 2011, **519**, 6459-6466.
39. N. Tsuboi, Y. Takahashi, S. Kobayashi, H. Shimizu, K. Kato and F. Kaneko, *J. Phys. Chem. Solids* 2003, **64**, 1671-1674.
40. D. G. Barton, M. Shtein, R. D. Wilson, S. L. Soled and E. Iglesia, *J. Phys. Chem. B* 1999, **103**, 630-640.
41. Z. Chen, T. F. Jaramillo, T. G. Deutsch, A. Kleiman-Shwarsctein, A. J. Forman, N. Gaillard, R. Garland, K. Takanabe, C. Heske, M. Sunkara, E. W. McFarland, K. Domen, E. L. Miller, J. A. Turner and H. N. Dinh, *J. Mater. Res.* 2010, **25**, 3-16.
42. G. Hitoki, A. Ishikawa, T. Takata, J. N. Kondo, M. Hara and K. Domen, *Chem. Lett.* 2002, **31**, 736-737.
43. P. T. Hsiao, Y. L. Tung and H. Teng, *J. Phys. Chem. C* 2010, **114**, 6762-6769.
44. J. N. Nian, C. C. Tsai, P. C. Lin and H. Teng, *J. Electrochem. Soc.* 2009, **156**, H567-H573.

45. P. S. Li and H. Teng, *J. Chin. Inst. Chem. Eng.* 2007, **38**, 267-273.

46. K. P. Wang and H. Teng, *Phys. Chem. Chem. Phys*. 2009, **11**, 9489-9496.

47. L. C. Wang and M. Tao, *Electrochem. Solid-State Lett.* 2007, **10**, H248-H250.

48. F. Zhang, A. Yamakata, K. Maeda, Y. Moriya, T. Takata,J. Kubota , K. Teshima, S. Oishi and K. Domen *J. Am. Chem. Soc.* 2012, **134**, 8348-8351.

49. J. Hou, Z. Wang, C. Yang, H. Cheng, S. Jiao and H. Zhu, *Energy Environ. Sci.* 2013, **6**, 3322-3330.

50. S. N. Inamdar, P. P. Ingole, and S. K. Haram, *ChemPhysChem* 2008, **9**, 2574-2579.

51. S. K. Haram, B. M. Quinn, and A. J. Bard, *J. Am. Chem. Soc.* 2001, **123**, 8860-8861.

52. J. Wang and F. E. Osterloh, *J. Mater. Chem. A* 2014, **2**, 9405-9411.

53. S. Banerjee, S. K. Mohapatra, P. P. Das and M. Misra, *Chem. Mater.* 2008, **20**, 6784-6791.

54. M. Radecka, M. Wierzbicka and M. Rekas, *Physica B* 2004, **351**, 121-123.

55. M. de Respinis, G. De Temmerman, I. Tanyeli, M.C.M. van de Sanden, R.P. Doerner, M.J. Baldwin and R. van de Krol, *ACS Appl. Mater. Interfaces* 2013, **5**, 7621-7625.

56. J.S. Moon, Y.W. Lee, S.B. Han, C.K. Zhoh and K.W. Park, *Int. J. Electrochem. Sci*. 2013, **8**, 6656-6663.

57. P. T. Hsiao and H. Teng, *J. Am. Ceram. Soc.* 2009, **92**, 888-893.

58. L. C. Chen, C. T. Hsieh, Y. L. Lee and H. Teng, *ACS Appl. Mater. Interfaces* 2013, **5**, 11958-11964.

59. J. Krüger, R. Plass, M. Grätzel, P. J. Cameron and L. M. Peter, *J. Phys. Chem. B* 2003, **107**, 7536-7539.

60. Y. J. Liou, P. T. Hsiao, L. C. Chen, Y. Y. Chu and H. Teng, *J. Phys. Chem. C* 2011, **115**, 25580-25589.

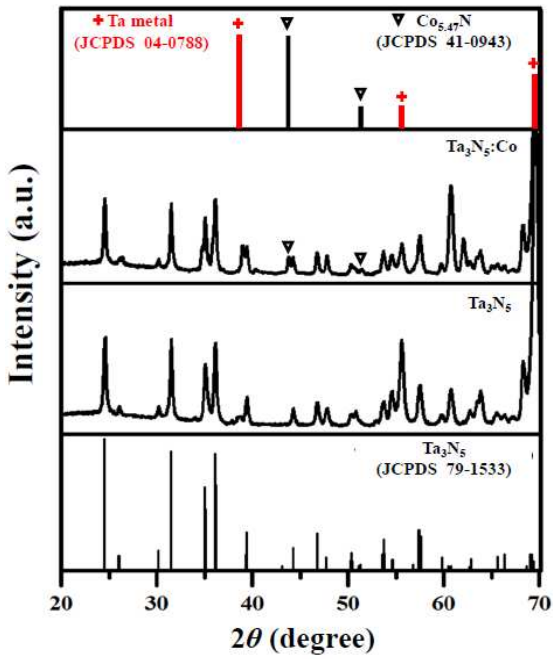

Figure 1. X-Ray diffraction patterns of Ta_3N_5 and Ta_3N_5:Co films obtained from nitridation in NH_3 at 950 °C for 2 h. The standard patterns of Ta metal, Ta_3N_5 and $Co_{5.47}N$ crystals are depicted in the lower and upper panels, respectively.

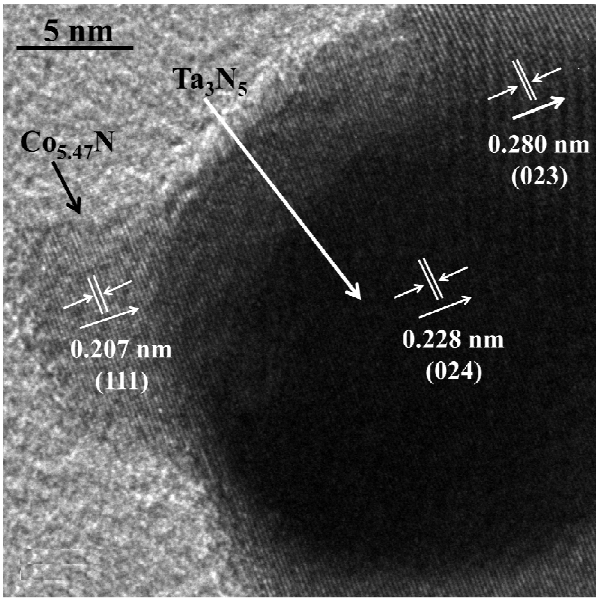

Figure 2. High-resolution TEM image of a Ta_3N_5:Co particulate specimen scraped from the as the synthesized Ta_3N_5:Co film. A small $Co_{5.47}N$ crystal was in intimate contact with a Ta_3N_5 particle.

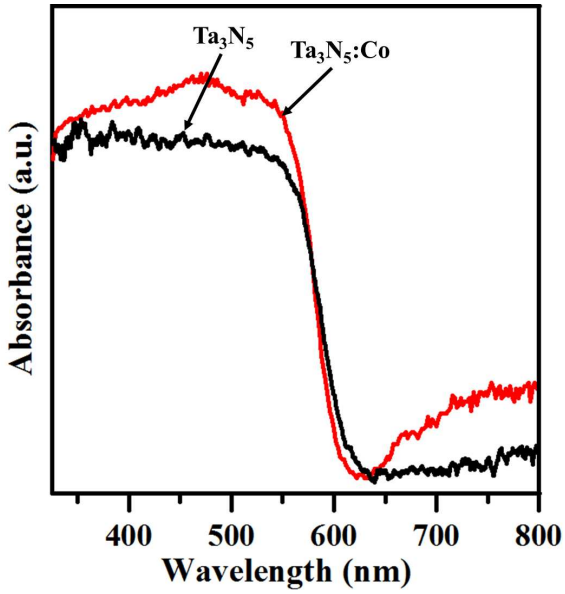

Figure 3. Diffuse reflectance spectra of the Ta_3N_5 and Ta_3N_5:Co films.

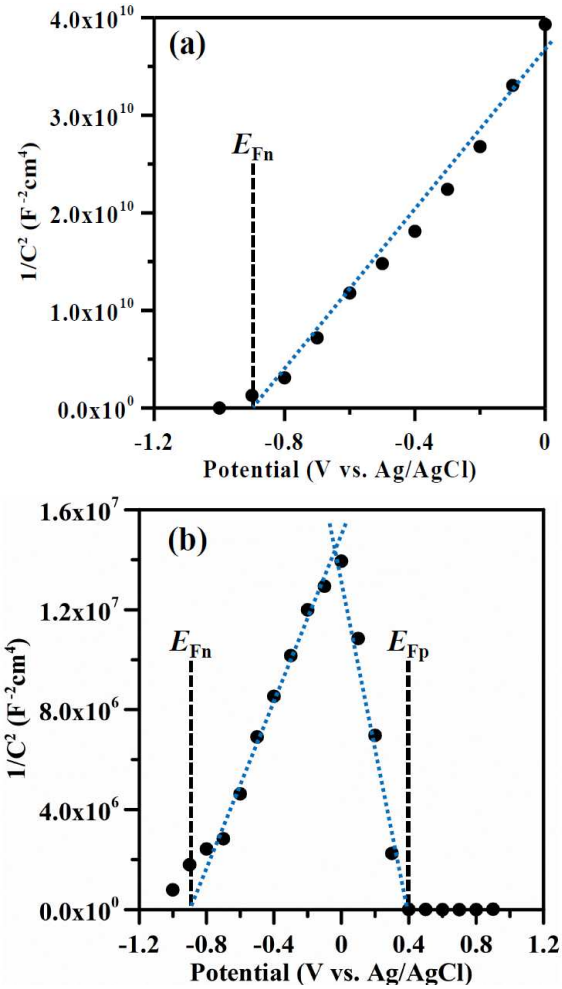

Figure 4. Variation of capacitance (*C*) with the applied potential in 0.5 M KOH presented in the Mott-Schottky relationship for different films: (a) Ta_3N_5; (b) Ta_3N_5:Co. The capacitance was determined by electrochemical impedance spectroscopy. The symbols E_{Fp} and E_{Fn} represent the Fermi levels of p- and n-type semiconductors.

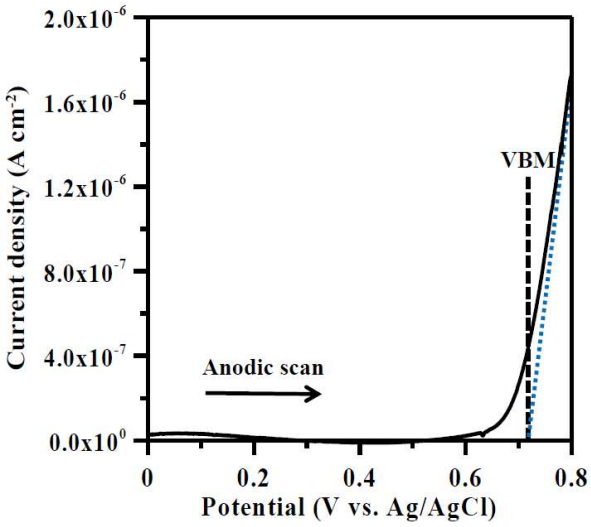

Figure 5. Anodic potential scan for determining the valance band maximum (VBM) of the n-type Ta_3N_5 at 10 mV s^{-1}.

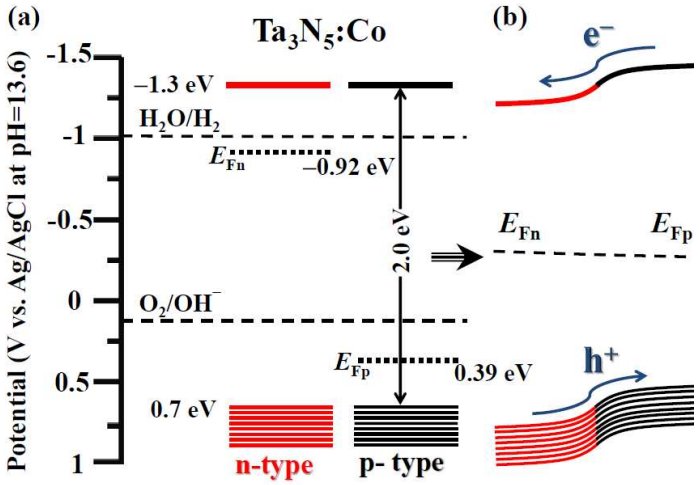

Figure 6. Schematic energy level diagrams of the n- and p-type domains in Ta_3N_5:Co in comparison with the potentials for water reduction and oxidation: (a) neutral situation before forming junction; (b) neutrality disturbed after forming junction. The junction creates a built-in electrical field to facilitate hole injection into the solution phase for O_2 evolution.

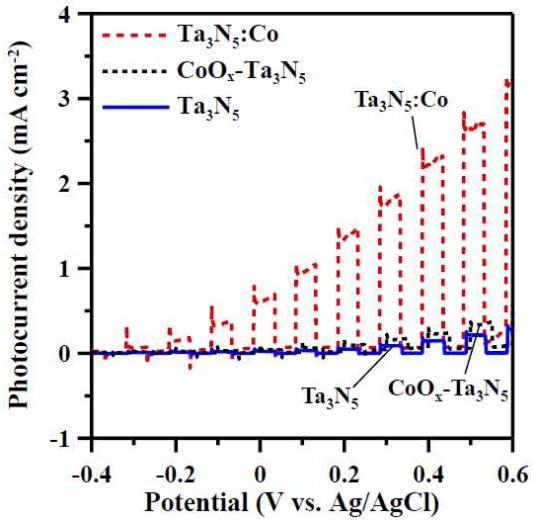

Figure 7. Current-potential characteristics of the Ta_3N_5 and Ta_3N_5:Co photoanodes with an anodic scan applied at 10 mV s^{-1} and illuminated with chopped AM 1.5G simulated sunlight at 100 mW cm^{-2}. The electrolyte is a 0.5-M KOH aqueous solution (pH=13.6). For the comparison purpose, this figure also shows the photocurrent of a CoO_x-deposited Ta_3N_5 film, which was obtained by loading Co ions only after the anodization process.

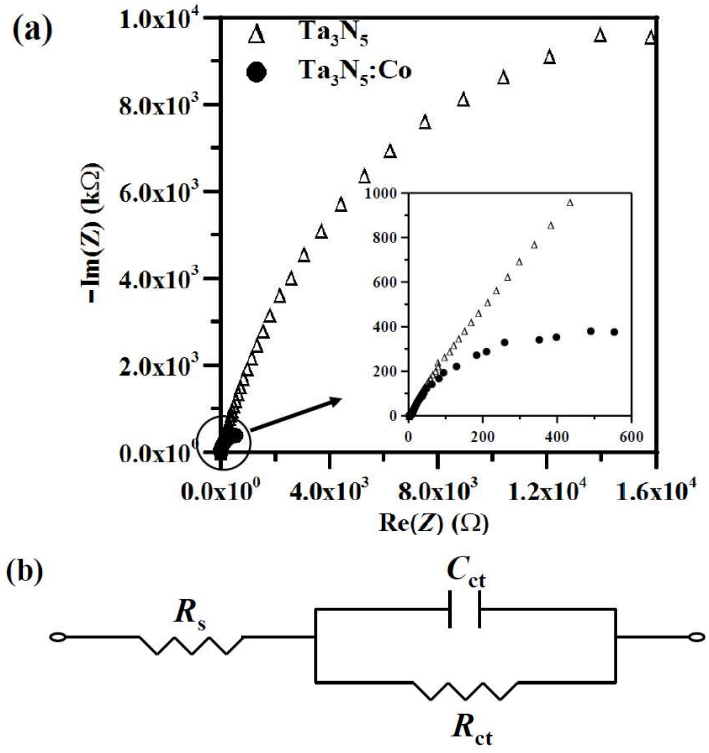

Figure 8. (a) Electrochemical impedance spectra of the Ta_3N_5 and Ta_3N_5:Co electrodes biased at 0.5 V (vs. Ag/AgCl) with an AC frequency range of 0.1-10^5 Hz. The electrodes were immersed in 0.5-M KOH aqueous solution and irradiated with AM 1.5G simulated sunlight (100 mW cm^{-2}). The inset show the magnification of the high-frequency region. (b) An equivalent circuit model for the photoanodes. R_s represents the solution resistance and the capacitance C_{ct} and resistance R_{ct} characterize the charge transfer behavior across the electrode-solution interface.

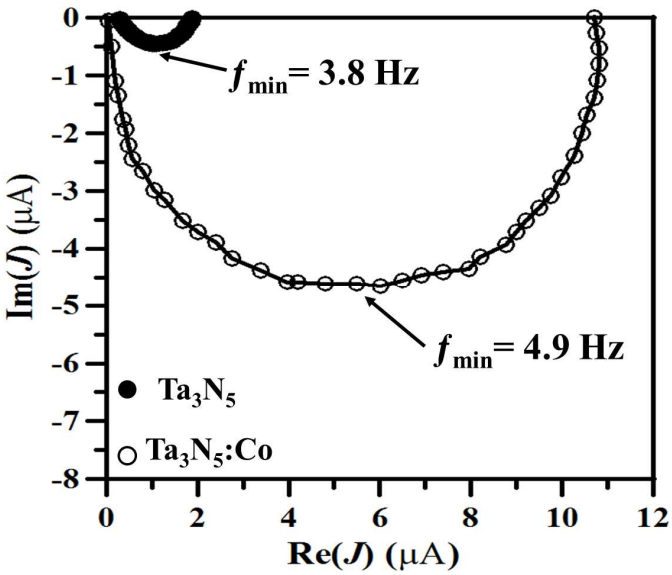

Figure 9. The IMPS responses of the Ta_3N_5 and Ta_3N_5:Co electrodes biased at 0.5 V (vs. Ag/AgCl) in a 0.5-M KOH aqueous solution. A blue light-emitting diode (λ_{max} = 455 nm) was used as the modulation light source with a dc intensity of 15 mW cm^{-2} and superimposed 5% AC intensity. The frequency at the Im(*J*) minimum (f_{min}) is indicated in the figure.

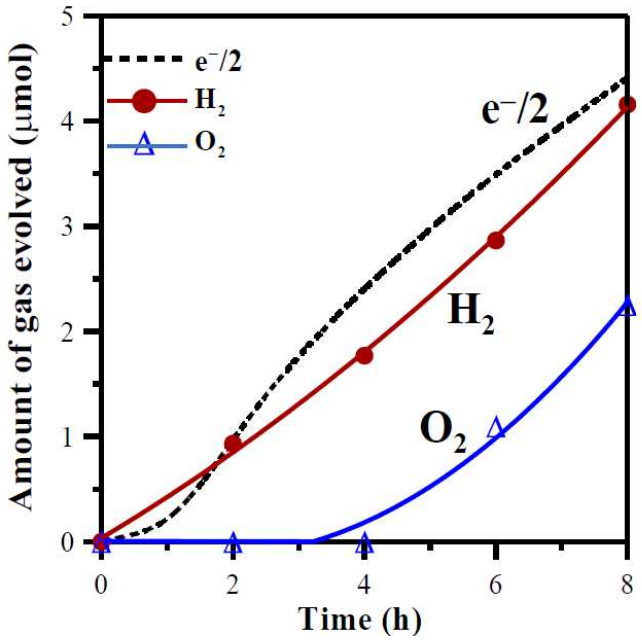

Figure 10. Time courses of H_2 and O_2 evolution from a photoelectrochemical system consisting of a Ta_3N_5:Co anode, a Pt-sheet cathode, and a 0.5-M KOH aqueous solution (pH=13.6) as the electrolyte, with an applied bias 0.8 V under visible light (800 nm > λ > 420 nm) irradiation at 49 mW cm^{-2}. This figure also shows the time course of the half amount of electrons passing through the external circuit ($e^-/2$).